

## Article

# Investigating Influential Parameters for High-Purity Germanium Crystal Growth

Sanjay Bhattarai, Dongming Mei \*, Narayan Budhathoki, Kunming Dong  and Austin Warren

Department of Physics, University of South Dakota, Vermillion, SD 57069, USA; sanjay.bhattarai@usd.edu (S.B.); narayan.budhathoki@coyotes.usd.edu (N.B.); kunming.dong@coyotes.usd.edu (K.D.); austin.warren@coyotes.usd.edu (A.W.)

\* Correspondence: dongming.mei@usd.edu

**Abstract:** This paper focuses on the research and development of high-purity germanium (HPGe) crystals for detector fabrication, specifically targeting applications in rare-event physics searches. The primary objective was to produce large-scale germanium crystals weighing  $>1$  kg with a controlled diameter of  $\sim 10$  cm and an impurity range of approximately  $10^{10}/\text{cm}^3$ . Ensuring structural integrity and excellent crystalline quality requires a thorough assessment of dislocation density, a critical aspect of the crystal development process. Dislocation density measurements play a crucial role in maximizing the sensitivity of HPGe detectors, and our findings confirmed that the dislocation density fell within acceptable ranges for detector fabrication. Additionally, this paper examines the segregation coefficient of various contaminants during the crystal development process. Comprehensive analysis of impurity segregation is essential for reducing contaminant quantities in the crystal lattice and customizing purification processes. This, in turn, minimizes undesired background noise, enhancing signal-to-noise ratios for rare-event physics searches and overall detector performance. The investigation included the segregation coefficients of three major acceptors and one donor in crystals grown at the University of South Dakota, providing valuable insights for optimizing crystal purity and detector efficiency.

**Keywords:** crystal growth; impurity segregation; dislocation density; net impurity concentration



**Citation:** Bhattarai, S.; Mei, D.; Budhathoki, N.; Dong, K.; Warren, A. Investigating Influential Parameters for High-Purity Germanium Crystal Growth. *Crystals* **2024**, *14*, 177. <https://doi.org/10.3390/cryst14020177>

Academic Editor: Wolfram Miller

Received: 25 January 2024

Revised: 5 February 2024

Accepted: 7 February 2024

Published: 10 February 2024



**Copyright:** © 2024 by the authors. Licensee MDPI, Basel, Switzerland. This article is an open access article distributed under the terms and conditions of the Creative Commons Attribution (CC BY) license (<https://creativecommons.org/licenses/by/4.0/>).

## 1. Introduction

One of the most perplexing mysteries of our world is the nature of dark matter, which is a fundamental question in particle physics beyond the Standard Model. Determining the characteristics of dark matter is therefore a major goal of underground physics. Several research groups are working on this project, utilizing a range of detection methods and materials [1–8]. Detectors with a very low energy threshold are required, because dark matter interacts with normal matter through a weakly elastic scattering process that only leaves a minimal energy deposition from nuclear or electronic recoils. Germanium (Ge) detectors provide the lowest energy threshold of all the detector technologies now in use, making them the most suitable for the hunt for dark matter. SuperCDMS [9,10], CoGeNT [6], CDEX [5], and EDELWEISS [8] are dark matter experiments using germanium detectors.

Due to their exceptional energy resolution and the ability to mitigate background interference from two neutrino double-beta ( $2\nu\beta\beta$ ) decay, high-purity Ge (HPGe) crystals serve as prominent detectors for investigating neutrinoless double-beta ( $0\nu\beta\beta$ ) decay. This experimental approach holds unique significance, as it stands as the sole method for ascertaining whether neutrinos possess Majorana properties. The exploration of  $0\nu\beta\beta$  decay serves as a crucial avenue for delving into new realms of physics, offering a sensitive probe into unresolved mysteries surrounding neutrinos, including their potential Dirac or Majorana nature, and contributing insights into fundamental questions like the observed excess of matter in the universe. Several research groups are using HPGe detectors to

find  $0\nu\beta\beta$  decay, including Majorana [11], GERDA [12], and a new effort by the LEGEND partnership [4], which aims to detect  $0\nu\beta\beta$  decay using tonne-scale  ${}^{76}\text{Ge}$  detectors in an ultra-low background environment. HPGe detectors can also be used to detect other rare-event physics searches like low-energy solar neutrinos, dark phonons, etc. [13].

The sensitivity of these detectors used for rare-event physics searches including dark matter,  $0\nu\beta\beta$  decay, solar neutrinos, dark photons, etc. is highly dependent on the purity of the Ge crystal used. The level of impurity can affect a detector's performance. For example, increasing the level of impurity will increase the detector noise and decrease energy resolution [14]. Therefore, in order to achieve the necessary sensitivity, HPGe detectors are needed, and these detectors can only be made through an intricate procedure that involves crystal growth and purification. From the purified Ge ingots, HPGe crystals can be grown using the Czochralski (CZ) process [15]. As part of the CZ process, purified Ge is melted in a crucible and utilized to make a single crystal. This crystal development method requires a seed crystal, and the crucible is constructed of high-purity quartz. The temperature (power) and the pull rate of the seed crystal are regulated during the CZ process, in order to produce a high-quality crystal. The Ge ingots inside the quartz crucible must reach a temperature slightly above  $937\text{ }^\circ\text{C}$ , sufficient to melt the ingots without significant evaporation. The pulling rate influences both the growth rate and the structural/electrical properties of the crystal. Diameter control is a critical challenge in HPGe growth via the CZ process. The crystal's structural integrity, electrical characteristics, and detector performance are directly influenced by its diameter. Maintaining a uniform diameter reduces electrical fluctuations, ensuring consistent crystal quality. This control is essential for fabricating detectors with optimal resolution and charge collection efficiency. Diameter variations can introduce non-uniformities and crystallographic defects, negatively impacting electrical characteristics and purity, ultimately leading to poor detector performance. The Lawrence Berkeley National Laboratory (LBNL), in collaboration with other US laboratories and industrial enterprises, played a pivotal role in pioneering the production of high-purity germanium, from as early as the 1970s [16,17]. Presently, commercial companies are capable of growing crystals of commendable quality, featuring impurity levels around  $(0.5\text{ to }3) \sim 10^{10}/\text{cm}^3$ , with masses reaching up to 4 kg and body diameters ranging from 8 to 10 cm [18,19].

Another crucial factor in detector-grade crystals is the dislocation density within the crystal. The detector grade crystal should have a dislocation density that ranges from  $3 \times 10^2/\text{cm}^2$  to  $10^4/\text{cm}^2$  [17,20]. This is achieved by making the neck of the crystal small and gradually increasing its size, also called the dash necking process [21].

Another important step in the fabrication of HPGe detectors is the impurity profile and segregation analysis of various donors and acceptors during the CZ HPGe crystal growth process. The electrical properties of a crystal are greatly influenced by the presence and distribution of impurities, such as donors and acceptors [22]. This has a direct impact on the crystal's suitability for detection applications. The net impurity level in the crystal is required to be in the range of not greater than  $5 \times 10^0/\text{cm}^3$  and less than  $3 \times 10^{10}/\text{cm}^3$  [23,24]. The net impurity concentration results from compensating various donor and acceptor impurities within the crystal. Each impurity exhibits a unique segregation behavior during the crystal growth process [22]. To attain the necessary net impurity concentration, desired electrical properties, effective charge transport, and high-resolution capabilities in detectors, it is crucial to comprehend and control the various impurity segregation factors.

The University of South Dakota (USD) has emerged as a new player in the development of HPGe crystals through the implementation of the CZ crystal growth process. Our successful demonstrations of growing HPGe crystals for fabrication into detectors [18,23,25–27] mark a significant progress. However, there remains ample room for improvement, particularly in the areas of diameter control, impurity profile, segregation behavior, and defect control.

This paper presents a recent investigation into HPGe crystal growth at USD, examining the diameter control and dislocation density of recently cultivated crystals. Additionally, we explore the segregation behavior of four major impurities—boron (B), aluminum (Al),

gallium (Ga), and phosphorous (P)—and estimate the quantity of each impurity in the locally grown crystal.

## 2. Materials and Methods

The commercially purchased ingots, initially possessing impurity levels of approximately  $\sim 10^{13}/\text{cm}^3$ – $10^{14}/\text{cm}^3$ , underwent purification through zone refinement to reduce impurity concentrations to the range of  $(2\text{--}3) \times 10^{11}/\text{cm}^3$  [28]. These refined ingots constituted the initial charge for the crystal. Cleaning involved deionized (DI) water and acetone to eliminate organic impurities, followed by a second DI water wash and etching with a Nitric acid and Hydrofluoric acid ( $\text{HNO}_3 : \text{HF}$ ) (3:1) solution to remove surface contaminants. The quartz crucibles and radiation glass shields used in crystal growth underwent cleaning with hydrogen peroxide ( $\text{H}_2\text{O}_2$ ) and drying with compressed nitrogen gas.

The raw materials, totaling 3665 g, were placed in a quartz crucible and melted using a pure graphite susceptor under radio frequency energy. Vacuum levels were increased to 6.9 Pa and then to roughly  $2 \times 10^{-3}$  Pa using a mechanical pump and diffusion pump, respectively. The melting process, spanning two hours, preceded crystal growth using the CZ technique. Germanium crystals, oriented along  $\langle 100 \rangle$  with a diameter of 8–8.5 cm, were grown at a pull rate of 40 mm/h for the neck portion and 22 mm/h for the remainder. Growth occurred in an ambient hydrogen atmosphere with a purity level (5N) at a flow rate of 150 L/h under 1 atm pressure.

Upon complete melting of the materials within the chamber, the input power was gradually reduced, inducing under-cooling and initiating the nucleation phase for crystal development. After achieving equilibrium, a rotating seed was carefully introduced to the melt, initiating the crystal growth process by gradually drawing the rod. Initially, the crystal's diameter was systematically increased into a conical shape to manage dislocation density—termed the Dash necking process [21]. As the crystal's neck and shoulder formed, power adjustments were made to control the diameter, maintaining consistency throughout the crystal's body. The tail portions were tapered to a smaller diameter. To prevent quartz crucible breakage, all the melt inside was carefully pulled out. After completion, a 10-h automated cooling schedule was employed, and once cooled, the crystal was extracted for characterization.

## 3. Result and Discussion

### 3.1. Diameter Control

The thermal field produced through induction heating in the crystal growth chamber is the main factor controlling the crystal's diameter. The crystal growth setup at USD includes a glass window for direct observation of the growing crystal. Furthermore, a camera on the furnace's top captures images, projected onto a computer screen. By monitoring the crystal's growth visually or through the computer, the diameter can be adjusted by regulating the applied power appropriately. The crystal's diameter ( $D$ ) is determined by the equation below [18,23]:

$$D = \sqrt{\frac{4dw/dt}{p\pi\rho_s + (dw/dt.\rho_s)/R^2\rho_L}} \quad (1)$$

In the equation,  $dw/dt$  represents the rate of change in weight over time,  $p$  is the pull rate,  $\rho_s$  and  $\rho_L$  are the densities of solid and liquid Ge, and  $R$  is the crucible radius. This equation is derived from the principle of conservation of mass, considering the liquid germanium in the crucible and the solidified mass of the crystal. It demonstrates that the crystal's diameter is directly proportional to its growth rate and inversely proportional to the pull rate of the seed. Figure 1 illustrates the power fluctuation with the position and growth rate during the crystal growth process, providing a means to control the crystal's diameter and adjust the power supply accordingly.

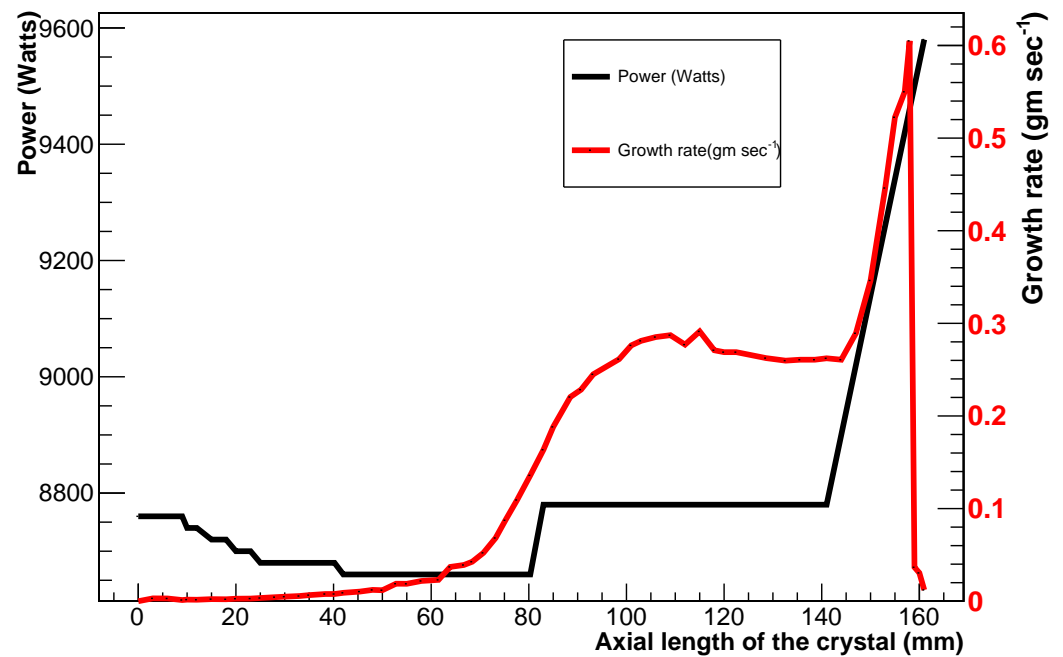


**Figure 1.** The input power and growth rate of the crystal along the axial direction of the growth. The red plot illustrates the crystal's growth rate in grams per second ( $\text{gm s}^{-1}$ ), indicating an increase in the growth rate within the neck portion and remaining almost constant along the body part, signifying a near-constant diameter in the body section. The black plot demonstrates the impact of input power on the crystal's growth rate.

As the power in the growth furnace increased, the temperature inside rose; conversely, a decrease in the growth rate resulted in a reduction in diameter. Initially, the equilibrium temperature was determined through trial and error, with a value set at 8780 Watts. To expand the crystal's neck when the seed was slowly pulled from the melt while rotating, the power was gradually lowered. The Dash neck technique proved effective in maintaining a small neck diameter and reducing dislocation density through gradually increasing the power. Once the neck had developed, as illustrated in Figure 1, the power was gradually reduced to lower the temperature of the growing furnace. This allowed the shoulder portion of the crystal to expand through increasing the diameter. Just before achieving the required diameter, the power was kept constant to maintain the temperature, and the body part was grown at this equilibrium temperature. Subsequently, the power was adjusted progressively to increase, leading to the growth of the tail portion of the crystal, as depicted in Figure 1. The tail part's diameter was gradually reduced, until all of the melt was removed from the crucible.

The diameter of the body part was meticulously controlled at approximately 8.5 cm, as depicted in Figure 2. Achieving precise control over the growth rate of the crystal toward the tail portion proved challenging, due to the difficulty in accurately determining the heat drawn by the solidified fraction of the crystal from the melt. Nevertheless, based on experience, we assumed a significant amount of heat loss from the melt to the solidified portion. To compensate for this, the input power was increased by 800 watts per hour, as illustrated in Figure 1, ensuring control over the diameter of the tail portion. The diameter of this section measured 11 cm. Given our objective of attaining a p-type detector-grade region in the body part, and considering that n-type impurities dominated the tail portion, the slightly larger diameter in the tail section did not pose a significant issue for our experiment.

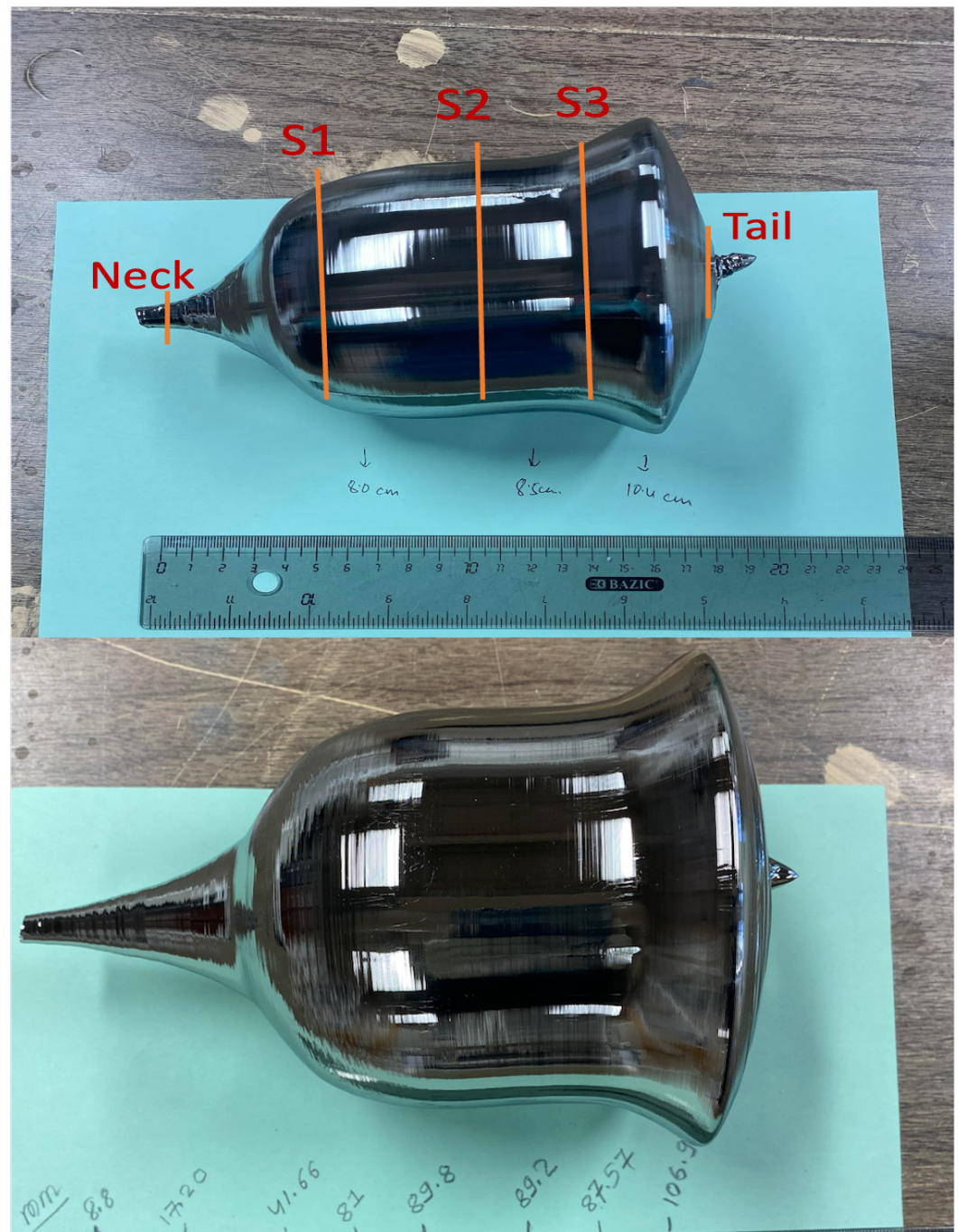


**Figure 2.** The crystal, cultivated at USD, underwent preparation for characterization. Samples were strategically cut from five distinct positions: neck; slices denoted as S1, S2, and S3; and the tail (**Top**). The crystal's diameter was measured at various positions along the axial direction using vernier calipers, with the diameter values depicted in millimeters (**bottom**).

Throughout the crystal growth process, we meticulously documented the crystal's position, corresponding weight, and applied input power. Utilizing the known pull rate of 22 mm/h and recorded weights at each position, we calculated the growth rate of the crystal,  $dw/dt$ , at each point. The crucible's diameter ( $2R$ ) was measured to be 18 cm. Employing these parameters, along with standard densities of solid and liquid Ge in Equation (1), enabled us to estimate the crystal's diameter at each position, as illustrated in Figure 3.

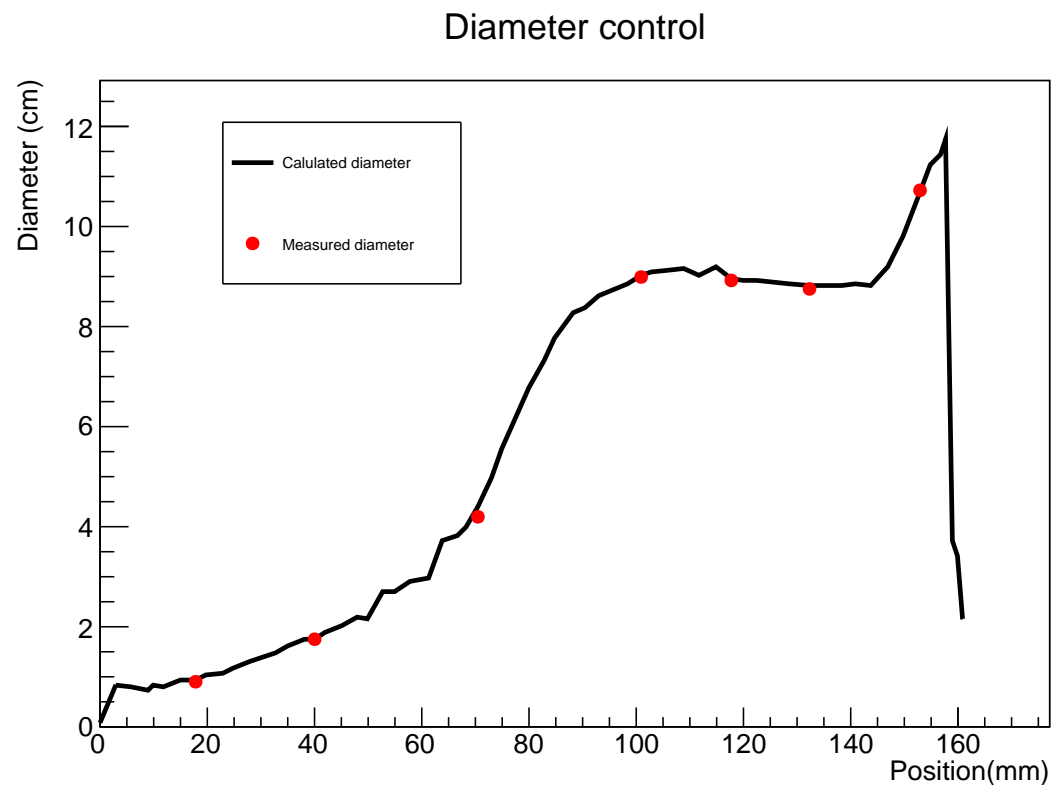


**Figure 3.** A comparison between the calculated diameter and the measured diameter for a crystal grown at USD is illustrated in Figure 3. The crystal's diameter underwent a gradual increase until it became constant in the body section. It remained at a constant diameter until it experienced a subsequent increase towards the near end portion, eventually tapering down at the tail.

The diameter of the grown crystal was measured at eight different positions using a vernier caliper, as depicted in Figure 2. A comparison between the calculated diameter using the growth rate and the measured actual diameter, shown in Figure 3, demonstrates our capability to estimate the crystal's diameter with less than 5% uncertainty during the crystal growth process. With such precision, we have consistently produced large-size HPGe crystals with well-controlled diameters in the USD lab.

### 3.2. Crystal Characterization

Upon completion of the crystal development process, the crystal was extracted from the chamber and subjected to characterization, to assess its compliance with the criteria for a detector-grade crystal. Two crucial properties are routinely measured: the dislocation density and the net impurity concentration at 77 K.

#### 3.2.1. Measurement of Impurities

The Hall effect measurement system, as outlined in [29], was employed to quantify the net impurity concentration. This involved segmenting the crystal into three slices along its body, denoted as S1, S2, and S3, as well as extracting samples from the neck and tail sections, as illustrated in Figure 2. The masses of the crystal portions cut from the neck, S1, S2, S3, and tail were measured at 18 g, 547 g, 1641 g, 2737 g, and 3631 g, respectively. Utilizing the ratio of these masses to the total crystal mass, we estimated the solidified fractions at different positions: 0.005 at the neck, 0.15 at S1, 0.45 at S2, 0.75 at S3, and 0.995 at the tail, which were used in the subsequent calculations. We selected the neck from the top part and the tail from the bottom part to assess the impurity distribution range in the crystal. The slice S1 was specifically chosen from the beginning of the body part of the crystal, a critical decision, as only the body part is utilized for detector fabrication, due to

its substantial diameter. Slice S2 was cut based on estimation, drawing from our experience in growing multiple crystals and insights from previous studies on high-purity crystals.

The wafers were subsequently sectioned into  $1.5 \times 1.5 \times 0.1 \text{ cm}^3$  samples, which underwent a meticulous process of polishing and etching using a solution of  $\text{HNO}_3 : \text{HF}$  in a 3:1 ratio. To facilitate measurements, four contacts were strategically established at the sample corners through the creation of indium gallium eutectic Ohmic contacts via scratching. The van der Pauw–Hall effect measurement system (Ecopia HMS-300 with a 0.5 Tesla permanent magnet) [25] was then employed for the assessment. Given that our detectors operated at 77K using liquid nitrogen, impurity measurements were conducted at the same temperature. This system allowed for the determination of not only impurity levels but also hole or electron mobility, resistivity, and the Hall coefficient. The net impurity level of the latest detector-grade crystal grown in the USD lab is presented in Table 1.

**Table 1.** The net impurity concentration, resistivity, and mobility of the HPGe crystal grown in the USD lab on 14 November 2023 are presented. The uncertainties for each measurement were determined within a 20% level, accounting for the accuracy in the Hall effect system.

Position	Net Impurity (/cm <sup>3</sup> )	Resistivity ( $\Omega \text{ cm}$ )	Mobility (cm <sup>2</sup> /Vs)
Neck	$1.01 \times 10^{11}$	$5.40 \times 10^2$	$3.24 \times 10^4$
S1	$6.31 \times 10^{10}$	$3.74 \times 10^3$	$3.63 \times 10^4$
S2	$1.55 \times 10^{10}$	$4.92 \times 10^3$	$3.48 \times 10^4$
S3	$-1.13 \times 10^{11}$	$3.80 \times 10^2$	$2.14 \times 10^4$
Tail	$-1.04 \times 10^{13}$	$6.32 \times 10^1$	$1.41 \times 10^4$

This table indicates that the segment between S1 and S2, of approximately 3.5 cm in thickness, 8.5 cm in diameter, and with a mass of 1043 g, is well-suited for detector fabrication. The mobility is contingent upon the concentration of impurities and other defects, such as dislocations. The compensation ratio (CR) of the crystal at the position  $g_i$  is defined as the ratio of n-type impurity (P) to the sum of the concentration of p-type impurities (B, Al, and Ga) at that position. In comparison to the mentioned paper, this crystal exhibited higher compensation ratios, ranging from 65–75% at the upper portion to 90–95% at the lower end. Consequently, the mobility of this crystal was lower than that reported in the referenced paper. Our experience with multiple crystal growths and detector fabrication suggests that these mobilities were more slightly diminished, due to elevated compensation ratios and dislocation densities, than usual but they still fell within acceptable ranges [16,24].

### 3.2.2. Dislocation Density Measurement

In a Ge crystal, the presence of hydrogen divacancy ( $V_2H$ ) is a common observation. To prevent the hydrogen divacancy from acting as a charge trapping center, it is crucial to maintain the dislocation density above  $3 \times 10^2/\text{cm}^2$  [17,20]. Conversely, if the dislocation density exceeds  $1 \times 10^4/\text{cm}^2$ , the dislocations themselves can act as trapping centers [17,20]. Therefore, the dislocation densities in the crystal should be carefully controlled within the range of  $3 \times 10^2/\text{cm}^2$  and  $1 \times 10^4/\text{cm}^2$  to fabricate high-quality detectors.

The dislocation density of a recent detector-grade crystal grown in the USD lab was measured using the etching pit counting technique. After slicing the grown crystals from four different positions (samples from the neck, S1, S2, and tail as labeled in the upper photo of Figure 2), they underwent polishing and etching with a solution of acetic acid: $\text{HNO}_3$ :HF (11:10:5) with 30 mg of dissolved iodine ( $I_2$ ). This etching process created small pits, to highlight dislocations under a microscope. The dislocation density was measured and observed using an Olympus BX 40 microscope. Each sample was placed under the optical microscope, and etch pits were counted at 10 different positions on the sample. The average

number of etch pits on the neck, S1, S2, and tail was found to be 4.7, 7.7, 12.4, and 25.4, respectively. The errors, calculated as about 10%, were determined by considering the minimum and maximum values in relation to the average. Sample photos of the etch pits seen under the microscope for each position are shown in Figure 4.

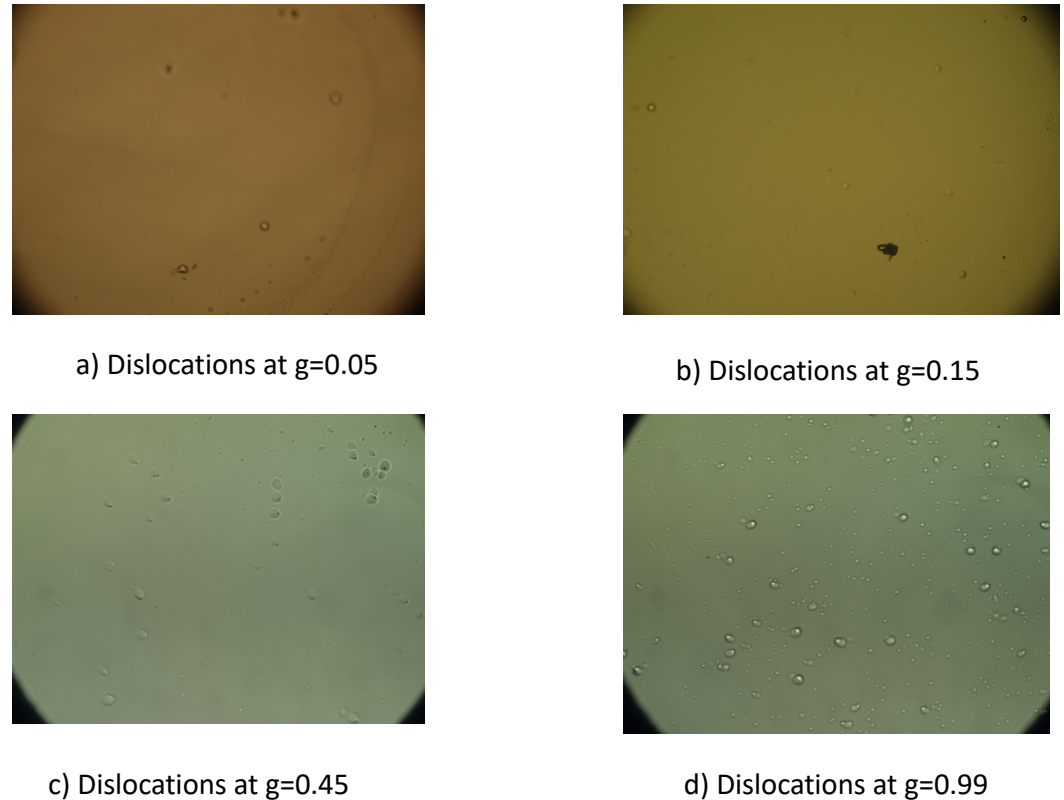


**Figure 4.** Optical microscope images depicting etch pits in samples from four different positions of the crystal. In these images, 'g' denotes the solidified portion of the crystal during the growth process.

The  $10\times$  lens covered a working area of  $0.0063\text{ cm}^2$ . Consequently, the dislocation density was calculated as  $746 \pm 7.46\text{ cm}^{-2}$  at the neck,  $1222.22 \pm 12.22\text{ cm}^{-2}$  at S1,  $1968.25 \pm 19.68\text{ cm}^{-2}$  at S2, and  $4031.74 \pm 40.31\text{ cm}^{-2}$  at the tail of the crystal, as illustrated in Figure 5. The observed dislocation density exhibited an increasing trend along the length of the crystal. However, it is important to note that the dislocation densities throughout the entire crystal grown in USD remained well within the acceptable range for detector fabrication.

### 3.3. Impurity Segregation Behavior Analysis

The equilibrium distribution coefficient, represented as  $K_0 = C/C_0$ , signifies the ratio of impurity concentration in the solid phase to that in the liquid phase, providing a measure of the equilibrium state in a solid/liquid system. In the past, the determination of equilibrium distribution coefficients involved reliance on phase diagram information or the slope of the solidus line to the liquidus [22]. Optimal distribution coefficients necessitate a crystal growth process characterized by rapid growth, slower rotation, and high diffusivity.

Appreciating the significance of the effective segregation coefficient,  $K_{eff}$ , for impurities in germanium is paramount, due to its direct influence on crucial growth parameters like melt convection velocity and RF coil stirring efficiency. FA Trumbore's study [30] delved into the equilibrium distribution coefficient of impurities in germanium at its melting point, providing valuable insights into this essential aspect of crystal growth.

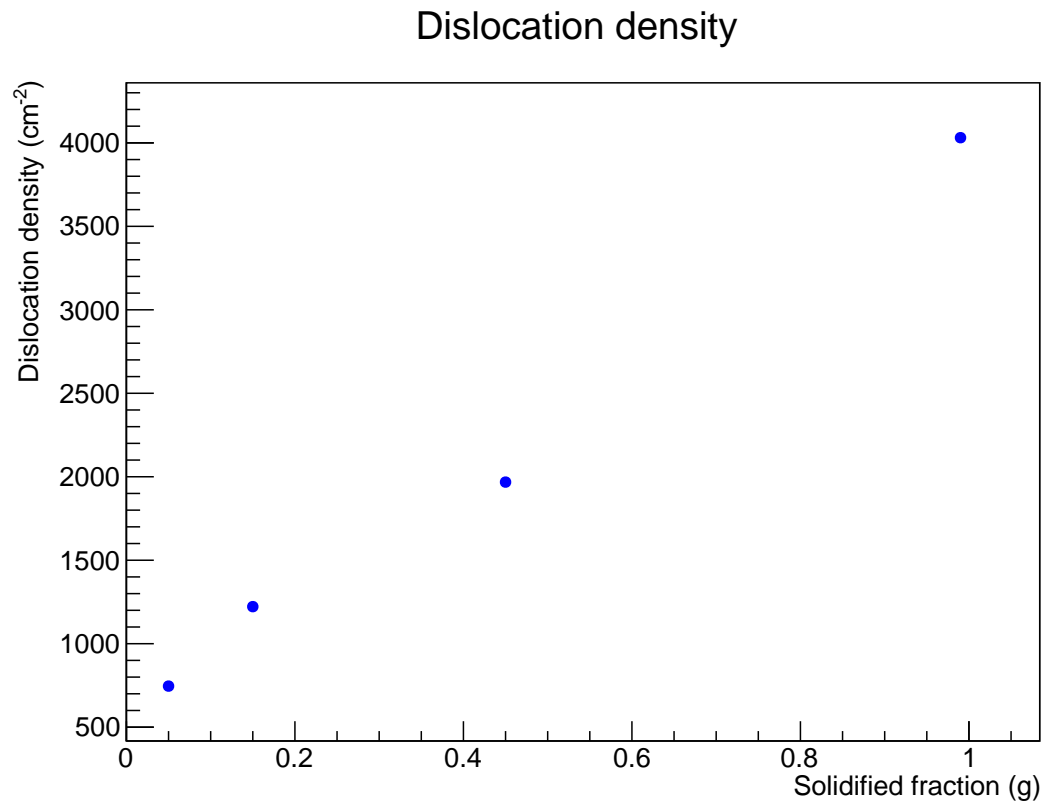


**Figure 5.** Dislocation density measurements at various positions along the axial direction of the crystal.

In a comprehensive investigation conducted by Wang et al. [24], photo-thermal ionization spectra (PTIS) measurements of a crystal grown at USD unveiled the presence of significant shallow-level impurities, specifically B, Al, Ga, and P. However, the specific concentration of each impurity and the compensation level remained undetermined. The primary objective of this study was to estimate the concentration of each of these impurities in a recently grown crystal. It is noteworthy that B, Al, and Ga acted as acceptor impurities, while P served as a donor impurity. The distribution of impurities within the HPGe crystal can be expressed as

$$C = C_0 K_{eff} (1 - g)^{(K_{eff}-1)}, \quad (2)$$

where  $C$  represents the impurity concentration in the crystal,  $C_0$  is the initial impurity concentration in the melt,  $g$  denotes the solidified fraction, and  $K_{eff}$  signifies the effective segregation coefficient. This equation elucidates that the segregation behavior of impurities in germanium is contingent upon the segregation coefficient of the impurities. Impurities with a segregation coefficient ( $k$ ) less than 1 tend to concentrate in the lower part of the crystal, whereas those with  $k$  greater than 1 have a propensity to accumulate in the upper part of the crystal. The calculation of the effective segregation coefficient is guided by the BPS model proposed by Burton, Prim, and Slichter [22], as shown below.

$$K_{eff} = \frac{K_0}{K_0 + (1 - K_0) \exp(-f\delta/D)}, \quad (3)$$

where  $K_0$  represents the equilibrium distribution coefficient,  $D$  is the impurity diffusion coefficient in the melt,  $\delta$  stands for the thickness of the diffusion boundary layer,  $f$  is the growth rate of an HPGe crystal. Additionally, the solute layer thickness, as per the BPS model, is expressed as

$$\delta = 1.6D^{1/3}v^{1/6}\omega^{-1/2}, \quad (4)$$

where  $D$  is the diffusivity of impurities at melt,  $\nu$  represents the kinematic viscosity,  $\mu/\rho$  stands for the dynamic viscosity/density of molten Ge, which equals  $1.35 \times 10^{-3} \text{ cm}^2/\text{s}$ , and  $\omega$  is the rotation rate of the crystal.

The diffusion coefficients for impurities  $B$  and  $Ga$  in Ge are  $3 \times 10^{-4} \text{ cm}^2/\text{s}$  [31] and  $7.2 \times 10^{-5} \text{ cm}^2/\text{s}$ , respectively [19]. Similarly, the diffusion coefficients for  $P$  and  $Al$  are  $5 \times 10^{-5} \text{ cm}^2/\text{s}$  [32] and  $6 \times 10^{-5} \text{ cm}^2/\text{s}$  [33,34], respectively. Using a crystal rotation rate of 3 rotations/min and Equation (4), the diffusion boundary layer thickness ( $\delta$ ) for  $B$ ,  $Ga$ ,  $Al$ , and  $P$  was calculated to be 0.159 cm, 0.098 cm, 0.093 cm, and 0.188 cm, respectively. The equilibrium distribution coefficients  $K_0$  for these impurities have been studied [30]. Using these values of  $K_0$ , the diffusion coefficients ( $D$ ), and a growth rate ( $f$ ) of 2.2 cm/h, in this experiment, we determined the effective segregation coefficients for  $B$ ,  $Ga$ ,  $Al$ , and  $P$  as 2.865, 0.201, 0.188, and 0.101, respectively. Subsequently, using these  $K_{eff}$  values in Equation (2), we plotted the ratio of  $C/C_0$  along the axial length of the crystal for all these impurities, as shown in Figure 6.

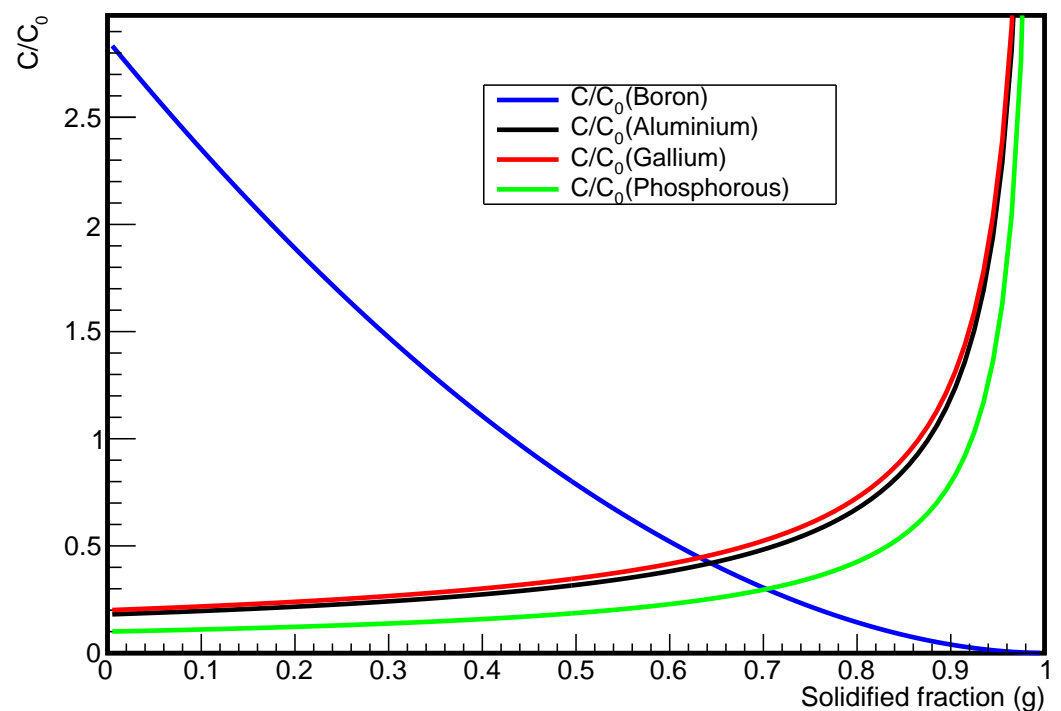


**Figure 6.** The ratio of the concentration of various impurities ( $C$ ) to their initial concentration in the melt ( $C_0$ ) along the crystal length is a crucial parameter in understanding the impurity distribution within a crystal.

The net impurity ( $C(g_i)$ ) obtained from the Hall effect measurement was the sum of all donor and acceptor impurities at the point  $g_i$  from where samples were cut. Therefore, the compensation model for the four different impurities is expressed as [35]:

$$C(g_i) = C_B(g_i) + C_{Al}(g_i) + C_{Ga}(g_i) - C_P(g_i). \quad (5)$$

We measured the  $C$  from four different positions ( $g_i$ ) of the crystal, as illustrated in Figure 2. Samples were cut from  $g = 0.5\%$ ,  $15\%$ ,  $75\%$ , and  $0.995\%$ . The values of  $g$  were determined by taking the ratio of the mass of a portion of the crystal cut to the total mass of the crystal, as discussed above. Plugging the values of  $C_B$ ,  $C_{Al}$ ,  $C_{Ga}$ , and  $C_P$  from Figure 6 and Equation (2) into Equation (5) with respective values of  $g_i$ , we obtain a system of four equations with four unknowns, which are

$$\begin{aligned}
2.84C_{0B} + 0.19C_{0Al} + 0.2C_{0Ga} - 0.10C_{0P} &= 1.01 \times 10^{11}, \\
2.12C_{0B} + 0.20C_{0Al} + 0.21C_{0Ga} - 0.11C_{0P} &= 6.31 \times 10^{10}, \\
0.22C_{0B} + 0.58C_{0Al} + 0.6C_{0Ga} - 0.35C_{0P} &= -1.13 \times 10^{11}, \\
0.00014C_{0B} + 13.89C_{0Al} + 13.87C_{0Ga} - 11.86C_{0P} &= -1.00 \times 10^{13},
\end{aligned} \tag{6}$$

where  $C_{0B}$ ,  $C_{0Al}$ ,  $C_{0Ga}$ ,  $C_{0P}$ , are the initial concentrations of B, Al, Ga, and P in the melt, respectively. The solution to these equations provides us with the initial concentration,  $C_0$ , for all the impurities under study. The initial concentrations of B, Al, Ga, and P for this crystal were found to be  $3.87 \times 10^{10}/\text{cm}^3$ ,  $2.21 \times 10^{11}/\text{cm}^3$ ,  $7.13 \times 10^{11}/\text{cm}^3$ , and  $1.89 \times 10^{12}/\text{cm}^3$ , respectively. Using these values of  $C_0$  and  $K_{eff}$  in Equation (2), we determined the concentration of impurities along the length of the crystal, as shown in Figure 7.

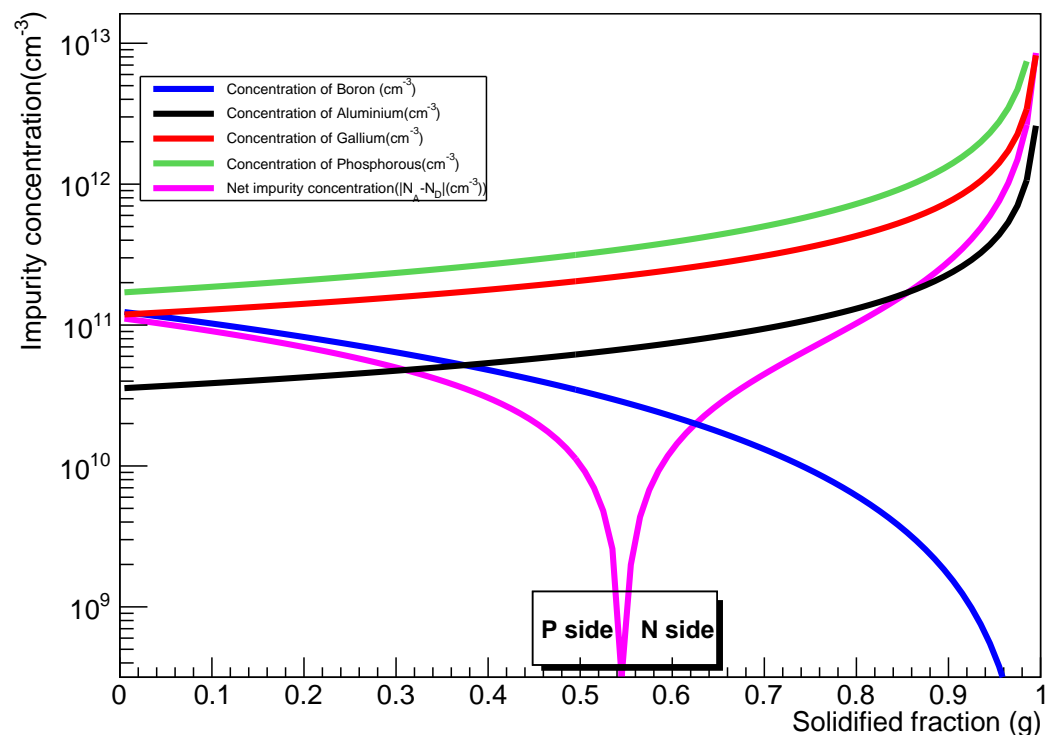


**Figure 7.** The estimated concentration of each impurity along the crystal length, as well as the net impurity concentration ( $|N_A - N_D|$ ), provide valuable insights into the distribution and overall impurity profile within the crystal. The net impurity concentration begins as p-type at the neck and gradually decreases until the solidified fraction of  $g = 0.542$ . After  $g = 0.524$ , the crystal transitions into n-type, as phosphorous (P) becomes the dominant impurity concentration within the crystal from this point onward.

While the effective segregation coefficient ( $K_{eff}$ ) of impurities depends on growth conditions and parameters such as rotation and pull rates, the values obtained in this study are reasonably consistent with prior works under similar growth conditions [16,19,36]. Notably, the segregation coefficient of Al remains elusive [16,17]. This work did not consider the formation of aluminum oxide (AlO), due to its highly complex segregation and diffusion behavior. Previous research suggested an effective segregation coefficient for AlO close to 1 [36]. Given the low pull and rotation rates and the hydrogen environment in the USD lab, the negligible oxygen content reaching the crystal body from the crucible walls led us to neglect AlO formation in our crystal compared to other impurities.

Estimating the amount of each impurity in the melt enhanced our understanding of crystal growth, ensuring quality, purity, and performance. This information is crucial

for current manufacturing processes and the advancement of crystal growth techniques, contributing to the production of large, HPGe crystals with homogeneous impurity profiles for efficient HPGe detectors [14]. Figure 7 illustrates the concentration of *B* decreasing along the crystal length, with most being segregated at approximately 50% of the crystal. Conversely, *Al*, *P*, and *Ga* exhibited normal segregation along the body, accumulating predominantly in the tail portion. The net impurity concentration of the crystal estimated at  $g = 0.45$  from Figure 7 was approximately  $1 \times 10^{10} / \text{cm}^3$ . In contrast, the net impurity concentration measured from the Hall effect measurements at the same position indicated an impurity level of  $\sim 1.55 \times 10^{10} / \text{cm}^3$ , as shown in Table 1. This disparity could be attributed to various factors, including the absence of precise diffusion coefficients for impurities in germanium melt, assumptions related to the ionization of all impurities during Hall effect measurements, and difficulties in accurately estimating the diffusion boundary layer at the crystal–melt interface. Addressing these challenges, coupled with investigations encompassing a diverse range of germanium crystals with varying impurity levels and doping, as well as exploring crystal growth under different parameters, could significantly enhance our comprehension of these impurities in future research.

#### 4. Conclusions

In the USD lab, we achieved successful growth of an HPGe crystal with a diameter of approximately 8.5 cm, yielding a substantial chunk of detector-grade material weighing around 1 kg. The dislocation density in this crystal fell within the acceptable range, measured at  $746 \text{ cm}^{-2}$  to  $4031 \text{ cm}^{-2}$ . Employing well-established methods, we determined the segregation coefficients for the four prominent impurities (B, Al, Ga, and P) in the crystal as 2.865, 0.188, 0.201, and 0.101, respectively. The initial concentrations of B, Al, Ga, and P in the crystal, as per our calculations, were  $3.87 \times 10^{10} / \text{cm}^3$ ,  $2.22 \times 10^{11} / \text{cm}^3$ ,  $7.13 \times 10^{12} / \text{cm}^3$ , and  $1.89 \times 10^{12} / \text{cm}^3$ , respectively. These values could elucidate the trends in net carrier concentrations. Additionally, we estimated the concentration of each impurity along the length of the crystal, providing valuable insights for future HPGe growth in the USD lab. Understanding the concentrations of the four major impurities in our crystal is instrumental for the growth of HPGe crystals, as this informs strategies involving doping or introducing a charge to enhance the material properties.

**Author Contributions:** Conceptualization, D.M. and S.B.; methodology, S.B., N.B., K.D. and A.W.; validation, D.M.; formal analysis, S.B.; investigation, N.B., K.D. and A.W.; resources, D.M.; data curation, S.B.; writing—original draft preparation, S.B.; writing—review and editing, S.B. and D.M.; visualization, S.B. and D.M.; supervision, D.M.; project administration, D.M.; funding acquisition, D.M. All authors have read and agreed to the published version of the manuscript.

**Funding:** This work was supported in part by NSF OISE 1743790, DE-SC0004768, and a governor’s research center supported by the State of South Dakota.

**Institutional Review Board Statement:** Not applicable.

**Data Availability Statement:** Data are contained within the article.

**Conflicts of Interest:** The authors declare no conflict of interest. The funders had no role in the design of the study; in the collection, analysis, or interpretation of data; in the writing of the manuscript; or in the decision to publish the results.

#### References

1. Agostini, M.; Allardt, M.; Andreotti, E.; Bakalyarov, A.; Balata, M.; Barabanov, I.; Barros, N.; Baudis, L.; Bauer, C.; Becerici-Schmidt, N.; et al. Production, characterization and operation of Ge enriched BE Ge detectors in GERDA. *Eur. Phys. J.* **2015**, *75*, 39. [CrossRef]
2. Agostini, M.; Bakalyarov, A.; Balata, M.; Barabanov, I.; Baudis, L.; Bauer, C.; Bellotti, E.; Belogurov, S.; Bettini, A.; Bezrukov, L.; et al. Probing Majorana neutrinos with double- $\beta$  decay. *Science* **2019**, *365*, 1445–1448. [CrossRef]
3. Agnese, R.; Anderson, A.; Aramaki, T.; Baker, W.; Balakishiyeva, D.; Banik, S.; Barker, D.; Thakur, R.B.; Bauer, D.; Binder, T.; et al. Nuclear-recoil energy scale in CDMS II silicon dark-matter detectors. *Nucl. Instruments Methods Phys. Res. Sect. Accel. Spectrometers Detect. Assoc. Equip.* **2018**, *905*, 71–81. [CrossRef]

4. Kermaidic, Y.; Radford, D. <sup>76</sup>Ge detector R&D Strategy for LEGEND. In Proceedings of the XXVIII International Conference on Neutrino Physics and Astrophysics, Heidelberg, Germany, 4–9 June 2018; p. 5. [[CrossRef](#)]
5. Yang, L.; Li, H.; Yue, Q.; Ma, H.; Kang, K.; Li, Y.; Wong, H.; Agartioglu, M.; An, H.; Chang, J.; et al. Search for Light Weakly-Interacting-Massive-Particle Dark Matter by Annual Modulation Analysis with a Point-Contact Germanium Detector at the China Jinping Underground Laboratory. *Phys. Rev. Lett.* **2019**, *123*, 221301. [[CrossRef](#)] [[PubMed](#)]
6. Aalseth, C.E.; Barbeau, P.S.; Colaresi, J.; Collar, J.; Leon, J.D.; Fast, J.E.; Fields, N.; Hossbach, T.W.; Knecht, A.; Kos, M.S.; et al. CoGeNT: A search for low-mass dark matter using p-type point contact germanium detectors. *Phys. Rev.* **2013**, *88*, 012002. [[CrossRef](#)]
7. Angloher, G.; Bauer, M.; Bavykina, I.; Bento, A.; Brown, A.; Bucci, C.; Ciemniak, C.; Coppi, C.; Deuter, G.; Von Feilitzsch, F.; et al. Commissioning run of the CRESST-II dark matter search. *Astropart. Phys.* **2009**, *31*, 270–276. [[CrossRef](#)]
8. Armengaud, E.; Augier, C.; Benoît, A.; Bergé, L.; Billard, J.; Broniatowski, A.; Camus, P.; Cazes, A.; Chapellier, M.; Charlieux, F.; et al. Searches for electron interactions induced by new physics in the EDELWEISS-III germanium bolometers. *Phys. Rev.* **2018**, *98*, 082004. [[CrossRef](#)]
9. Agnese, R.; Anderson, A.J.; Asai, M.; Balakishiyeva, D.; Thakur, R.B.; Bauer, D.; Beaty, J.; Billard, J.; Borgland, A.; Bowles, M.; et al. Search for low-mass weakly interacting massive particles with SuperCDMS. *Phys. Rev. Lett.* **2014**, *112*, 241302. [[CrossRef](#)] [[PubMed](#)]
10. Agnese, R.; Aralis, T.; Aramaki, T.; Arnquist, I.; Azadbakht, E.; Baker, W.; Banik, S.; Barker, D.; Bauer, D.; Binder, T.; et al. First dark matter constraints from a SuperCDMS single-charge sensitive detector. *Phys. Rev. Lett.* **2018**, *121*, 051301. [[CrossRef](#)]
11. Arnquist, I.; Avignone III, F.; Barabash, A.; Barton, C.; Barton, P.; Bhimani, K.; Blalock, E.; Bos, B.; Busch, M.; Buuck, M.; et al. Final Result of the Majorana Demonstrator’s Search for Neutrinoless Double- $\beta$  Decay in Ge 76. *Phys. Rev. Lett.* **2023**, *130*, 062501. [[CrossRef](#)] [[PubMed](#)]
12. Agostini, M.; Araujo, G.; Bakalyarov, A.; Balata, M.; Barabanov, I.; Baudis, L.; Bauer, C.; Bellotti, E.; Belogurov, S.; Bettini, A.; et al. Final results of GERDA on the search for neutrinoless double- $\beta$  decay. *Phys. Rev. Lett.* **2020**, *125*, 252502. [[CrossRef](#)]
13. She, Z.; Jia, L.; Yue, Q.; Ma, H.; Kang, K.; Li, Y.; Agartioglu, M.; An, H.; Chang, J.; Chen, J.; et al. Direct detection constraints on dark photons with the cdex-10 experiment at the china jinping underground laboratory. *Phys. Rev. Lett.* **2020**, *124*, 111301. [[CrossRef](#)] [[PubMed](#)]
14. Mei, D.; Mukund, R.; Wei, W.; Panth, R.; Liu, J.; Mei, H.; Li, Y.; Acharya, P.; Bhattarai, S.; Kooi, K.; et al. Impact of charge trapping on the energy resolution of Ge detectors for rare-event physics searches. *J. Phys. Nucl. Part. Phys.* **2020**, *47*, 105106. [[CrossRef](#)]
15. Czocharalski, J. Ein neues verfahren zur messung der kristallisationsgeschwindigkeit der metalle. *Z. für Phys. Chem.* **1918**, *92*, 219–221. [[CrossRef](#)]
16. Haller, E.E.; Hansen, W.L. Impurities in high-purity germanium as determined by Fourier transform spectroscopy. *IEEE Trans. Nucl. Sci.* **1974**, *21*, 279–286. [[CrossRef](#)]
17. Haller, E.E.; Hansen, W.; Hubbard, G.; Goulding, F. Origin and control of the dominant impurities in high-purity germanium. *IEEE Trans. Nucl. Sci.* **1976**, *23*, 81–87. [[CrossRef](#)]
18. Wang, G.; Mei, H.; Mei, D.; Guan, Y.; Yang, G. High purity germanium crystal growth at the University of South Dakota. In *Journal of Physics: Conference Series*; IOP Publishing: Bristol, UK, 2015; Volume 606, p. 012012.
19. Subramanian, A.; Abrosimov, N.; Gybin, A.; Gugushev, C.; Juda, U.; Fiedler, A.; Bärwolf, F.; Costina, I.; Kwasniewski, A.; Dittmar, A.; et al. Investigation of Doping Processes to Achieve Highly Doped Czocharalski Germanium Ingots. *J. Electron. Mater.* **2023**, *1–11*. [[CrossRef](#)]
20. Hansen, W. High-purity germanium crystal growing. *Nucl. Instruments Methods* **1971**, *94*, 377–380. [[CrossRef](#)]
21. Dash, W. Improvements on the pedestal method of growing silicon and germanium crystals. *J. Appl. Phys.* **1960**, *31*, 736–737. [[CrossRef](#)]
22. Burton, J.; Prim, R.; Slichter, W. The distribution of solute in crystals grown from the melt. Part I. Theoretical. *J. Chem. Phys.* **1953**, *21*, 1987–1991. [[CrossRef](#)]
23. Wang, G.; Sun, Y.; Yang, G.; Xiang, W.; Guan, Y.; Mei, D.; Keller, C.; Chan, Y.D. Development of large size high-purity germanium crystal growth. *J. Cryst. Growth* **2012**, *352*, 27–30. [[CrossRef](#)]
24. Wang, G.; Amman, M.; Mei, H.; Mei, D.; Irmscher, K.; Guan, Y.; Yang, G. Crystal growth and detector performance of large size high-purity Ge crystals. *Mater. Sci. Semicond. Process.* **2015**, *39*, 54–60. [[CrossRef](#)]
25. Raut, M.S.; Mei, H.; Mei, D.M.; Bhattarai, S.; Wei, W.Z.; Panth, R.; Acharya, P.; Wang, G.J. Characterization of high-purity germanium (Ge) crystals for developing novel Ge detectors. *J. Instrum.* **2020**, *15*, T10010. [[CrossRef](#)]
26. Bhattarai, S.; Panth, R.; Wei, W.Z.; Mei, H.; Mei, D.M.; Raut, M.S.; Acharya, P.; Wang, G.J. Investigation of the electrical conduction mechanisms in P-type amorphous germanium electrical contacts for germanium detectors in searching for rare-event physics. *Eur. Phys. J.* **2020**, *80*, 1–10. [[CrossRef](#)]
27. Meng, X.H.; Wang, G.J.; Wagner, M.D.; Mei, H.; Wei, W.Z.; Liu, J.; Yang, G.; Mei, D.M. Fabrication and characterization of high-purity germanium detectors with amorphous germanium contacts. *J. Instrum.* **2019**, *14*, P02019. [[CrossRef](#)]
28. Yang, G.; Guan, Y.; Jian, F.; Wagner, M.; Mei, H.; Wang, G.; Howard, S.; Mei, D.; Nelson, A.; Marshal, J.; et al. Zone refinement of germanium crystals. In *Journal of Physics: Conference Series*; IOP Publishing: Bristol, UK, 2015; Volume 606, p. 012014.
29. Hall, E.H. XVIII. On the “Rotational Coefficient” in nickel and cobalt. *Lond. Edinb. Dublin Philos. Mag. J. Sci.* **1881**, *12*, 157–172. [[CrossRef](#)]

30. Trumbore, F.A. Solid solubilities of impurity elements in germanium and silicon. *Bell Syst. Tech. J.* **1960**, *39*, 205–233. [[CrossRef](#)]
31. Taishi, T.; Murao, Y.; Ohno, Y.; Yonenaga, I. Segregation of boron in germanium crystal. *J. Cryst. Growth* **2008**, *311*, 59–61. [[CrossRef](#)]
32. Kodera, H. Constitutional supercooling during the crystal growth of germanium and silicon. *Jpn. J. Appl. Phys.* **1963**, *2*, 527. [[CrossRef](#)]
33. Becker, M.; Kargl, F.; Bührig-Polaczek, A. Solidification Kinetics in Al-Cu and Al-Ge Alloys Investigated by In-Situ X-ray Radiography. Technical Report; Fachgruppe für Materialwissenschaft und Werkstofftechnik. 2017. Available online: <https://publications.rwth-aachen.de/record/709136/files/709136.pdf> (accessed on 24 January 2024).
34. Becker, M.; Klein, S.; Kargl, F. Free dendritic tip growth velocities measured in Al-Ge. *Phys. Rev. Mater.* **2018**, *2*, 073405. [[CrossRef](#)]
35. Abrosimov, N.; Czupalla, M.; Dropka, N.; Fischer, J.; Gybin, A.; Irmscher, K.; Janicskó-Csáthy, J.; Juda, U.; Kayser, S.; Miller, W.; et al. Technology development of high purity germanium crystals for radiation detectors. *J. Cryst. Growth* **2020**, *532*, 125396. [[CrossRef](#)]
36. Haller, E.E.; Hansen, W.L.; Goulding, F.S. Physics of ultra-pure germanium. *Adv. Phys.* **1981**, *30*, 93–138. [[CrossRef](#)]

**Disclaimer/Publisher’s Note:** The statements, opinions and data contained in all publications are solely those of the individual author(s) and contributor(s) and not of MDPI and/or the editor(s). MDPI and/or the editor(s) disclaim responsibility for any injury to people or property resulting from any ideas, methods, instructions or products referred to in the content.